ARTICLE

JAAS
www.rsc.org/jaas

Space- and time-resolved dynamics of plasmas generated by laser double pulses interacting with metallic samples†

Reinhard Noll, Ralph Sattmann, Volker Sturm and Stefan Winkelmann

Fraunhofer-Institut für Lasertechnik (ILT), Steinbachstrasse 15, 52074 Aachen, Germany. E-mail: reinhard.noll@ilt.fraunhofer.de; Fax: 49 241 8906 121; Tel: 49 241 8906 0

Received 8th December 2003, Accepted 11th March 2004
First published as an Advance Article on the web 19th March 2004

Significant improvements to the analytical performance of laser-induced breakdown spectrometry (LIBS) were achieved by the use of laser double pulses to ablate and excite the sample material to be analysed. To clarify the underlying physical phenomena the dynamics of the laser-induced plasma in air is studied using a high-speed electro-optic camera to observe the spatial and temporal development of the plasma geometry. A Mach–Zehnder interferometer was set-up to detect the spatio-temporal changes of the refractive index of the plasma. The velocities of the luminous plasma front and shock waves after the impact of the first laser pulse are consistent with the prediction of Sedov's model for spherical expansion. The dynamics caused by the second laser pulse of the double pulse differ significantly, indicating a modified state of the local atmosphere in the interaction region. Electron densities determined interferometrically amount to about 3×10^{18} cm^{-3} at the center of the hemispheric plasma geometry at a delay time of 2 μs. Whereas the electron density for single or double pulses is approximately the same, the volume of the plasma is greater by more than a factor of 3 after the interaction with the double pulse of the same total energy.

1. Introduction

The dominant excitation source for laser-induced breakdown spectrometry (LIBS) is single Q-switched pulses generated by pulsed solid state lasers.[1–5] These pulses have, typically, a width (FWHM) in the range of 5–20 ns. The repetition rate amounts to 2–50 Hz for flashlamp-pumped lasers. Double pulses and multiple-pulses were studied to improve the analytical performance of LIBS, for instance for the determination of traces in metallic matrices or to enable special applications such as, for example, the analysis of samples under water,[6–10] or to increase the ablation rate in laser material processing.[11] The term "double pulse" is defined here as follows: two laser pulses each having a width in the range of about 5–30 ns, which are separated in time by several 100 ns up to several microseconds. This interpulse separation is denoted by Δt in the following. Several methods are available to generate these double pulses: (a) a single pulsed laser with a modified electronic control of the Q-switch to generate two pulses within a single flashlamp discharge, (b) superposition of the beams of two pulsed lasers. For case (a) only one laser is necessary and the two pulses are emitted collinearly. However, the interpulse separation is limited to about 0.5 μs $< \Delta t <$ 180 μs. Case (b) requires two lasers and and a precise adjustment of the spatial superposition of the two pulses. This approach offers a high flexibility in terms of the wavelengths of the pulses, the pulse widths and the sequence of pulses. Fig. 1 illustrates schematically the various configurations studied so far for LIBS with double pulses. The arrows depict the direction of propagation of the laser pulses, the numbers show the temporal sequence. In the collinear case both pulses have the same axis of propagation and are directed orthogonally to the sample surface.[6–9] Various pulse combinations in terms of different wavelengths and different pulse widths have been studied.[10,11] In the case of orthogonal pre-ablation a first laser pulse is irradiated parallel to the sample surface, generating a laser-induced plasma above the sample surface in the ambient atmosphere, and the second pulse is directed orthogonally to the sample surface.[12] For orthogonal re-heating the sequence of the pulses is exchanged, *i.e.*, the laser pulse irradiates the sample at first and then the re-heating pulse propagating parallel to the sample surface is applied.[13] In the dual pulse crossed beam approach the first laser pulse is split into two beams, irradiating the sample under an angle of incidence of 45°; the second pulse follows in the same directions.[14]

Investigations of collinear double pulses[6,15] and triple pulses[8] generated within a single flashlamp discharge of a Nd:YAG laser for plasma excitation showed a significant improvement of the detection limits. With this approach detection limits for the elements C, P, S, Mn, Ni and Cr in low-alloy solid steel samples of less than 10 μg g^{-1} were achieved for the first time using LIBS. In a recent paper a LOD of 5 μg g^{-1} has been reported for the direct analysis of trace elements in liquid steel using a collinear triple-pulse configuration.[16]

Collinear double and multiple pulses lead to a significant increase of the ablated mass.[6] Comparing the ablated mass of a steel target using double pulses with 2×40 mJ and $\Delta t = 6$ μs with a single pulse of 1×80 mJ yields an increase of about a factor of 2.5. Whereas for single pulses the ablated mass strongly saturates with increasing pulse energy, no such

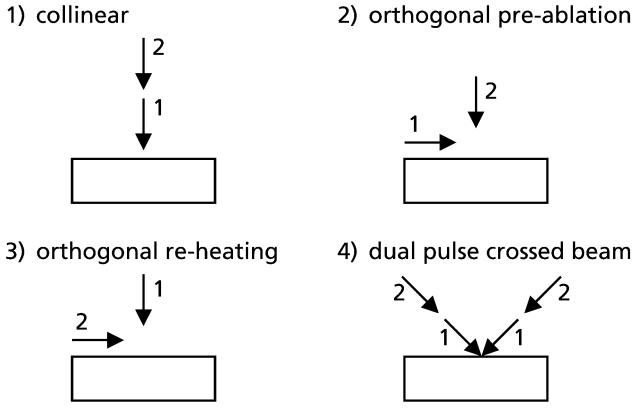

Fig. 1 Double pulse configurations studied for LIBS. The arrows depict the laser pulses and their direction of propagation and the numbers 1, 2 their temporal sequence.

† Presented at the Second Euro-Mediterranean Symposium on Laser Induced Breakdown Spectroscopy, Hersonissos, Crete, Greece, September 30th–October 3rd, 2003.

DOI: 10.1039/b315718k

saturation behaviour is observed for double and multiple pulses up to burst energies (denoting the sum of pulse energies within a double or multiple pulse) of 320 mJ. Electron temperatures in the laser-induced plasma determined spectroscopically are higher by 1000 K to 1500 K using double pulses with respect to those measured in the plasmas generated by single pulses of the same energy (*i.e.*, the energy of the single pulse is equal to the total energy of the double pulse). Hence the increased line emission observed using double pulse excitation is linked with the greater mass ablated and the higher temperatures achieved in the laser-induced plasma.[6]

For collinear double pulses studied for the analysis of solid metallic samples under water an increase of the ablated mass of aluminium samples by a factor of 3.8 was reported.[7] The observed increase of line emissions is attributed to the formation of a bubble in the water layer above the sample surface generated by the first pulse into which the emitting atoms can expand. Owing to the absence of atomic emissions from the plasma produced by the single pulse it was not possible to determine the temperature and electron density for underwater excitation. The authors conclude that in this case the temperature is less than 3000 K. For double pulse excitation an electron temperature of 8900 K was determined.[7]

Studies of collinear double pulses interacting with aluminium samples in air showed higher line intensities lasting longer than corresponding emissions generated by single laser pulses.[9] The time evolution of the line emission follows an exponential decay, where the decay time constant for the Al II line 624.34 nm and double pulse excitation is more than twice that determined for single pulse excitation. Looking at the ionic nitrogen emission N II at 500.1 nm revealed greater line intensities in the case of single pulse excitation than for double pulses, indicating that the pre-plasma formation induced by the first pulse reduces the air present nearby the surface and hence the concentration of nitrogen available for emission.[9]

In the orthogonal pre-ablation configuration an enhancement of Fe lines of about a factor 30 was observed comparing pre-ablation double pulses with single pulses.[12] A temperature increase by up to 5000 K was observed for pre-ablation double pulses. The signal enhancement is correlated with an increased crater volume, *i.e.*, the ablated mass is greater for pre-ablation double pulses than for single pulses.[12]

From a practical point of view, the collinear configuration is the most simple approach for double pulses, offering an easy access to the sample to be analysed. Hence, the investigations presented in this paper are focused on the collinear double pulse configuration. The aim of the investigations is to clarify the underlying physical processes of the observed improvements achieved with collinear double pulses, studying the space- and time-resolved dynamics of the plasmas generated by laser double pulses interacting with metallic samples. The experimental methodology is based on high-speed framing and streak images to observe the spatial and temporal development of the plasma using the optical emission of the plasma. Furthermore the spatio-temporal changes of the refractive index of the plasma are investigated using a Mach–Zehnder interferometer, where the shifts of the interference fringes are detected with a high-speed electro-optic camera.

2. Experiment

The experimental set-up for the time-resolved photography of the luminous laser-induced plasma is shown in Fig. 2. A Nd:YAG laser (Lumonics, Model HY 1200, modified) with multi-pulse option, operated at 10 Hz and 1064 nm emission wavelength, is used to generate the plasmas on the surface of a plane metallic sample in ambient air. Details of the laser are described in ref. 8. For the experiments presented in this paper, the plasma dynamics resulting from the laser-sample

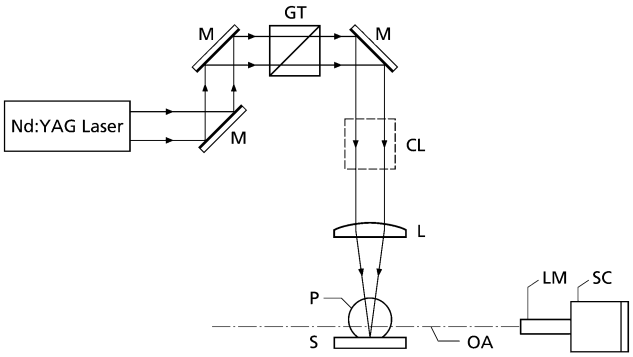

Fig. 2 Experimental set-up for high-speed photography of the luminous laser-induced plasma. M, Mirror; GT, Glan–Thompson polarizer; CL, volume absorbing disc calorimeter; L, lens; P, laser-induced plasma; S, sample; OA, optical axis of streak camera; LM, long distance microscope; SC, streak camera.

interaction with single and double Q-switched Nd:YAG laser pulses is investigated. The pulse width of a single pulse amounts to $\sim$15 ns, whereas each pulse of a double pulse has a width of $\sim$25 ns. In the case of double pulses the energy ratio adjusted is 1 : 1. The interpulse separation of the double pulses amounts to $\Delta t = 6$ μs. The pulses are focused by a planoconvex lens of 200 mm focal length on pure iron targets (Fe concentration > 99.99%). The beam waist of the laser focus lies inside the sample, 5 mm beneath its surface ($\Delta s = 5$ mm). The diameter of the laser beam on the surface of the sample is 280 μm. The pulse energies are adjusted by use of a Glan–Thompson polarizer and measured with a volume absorbing disc calorimeter (Scientech 38-0101). The optical axis of the streak camera is oriented perpendicularly to the propagation direction of the laser beam irradiating the sample. The laser-induced plasma is imaged by a long distance microscope on the streak camera (Hadland, Model Imacon 790) with an S 20 photocathode having the dimensions 9×8 mm^2. The distance between the laser-induced plasma and the front end of the microscope is about 160 mm. The streak camera can be operated in framing mode and in streak mode. In streak mode the slit of the streak camera is oriented collinearly to the propagation axis of the irradiated laser beam. The magnification object-to-image was determined using a line graticule placed at the position of the laser propagation axis just above the sample and observed with the streak camera in the focus mode. The experiments are carried out under normal atmospheric conditions.

The experimental set-up used for the interferometric investigations is shown schematically in Fig. 3. The components to generate the laser-induced plasma are identical to Fig. 2, but the sample is now located in a gas tight measuring chamber allowing experiments with air pressures of $p_0 = 100$ mbar and 1013 mbar. The Mach–Zehnder interferometer is oriented in such a way that one arm passes through the interaction volume above the sample surface perpendicular to the irradiated Nd:YAG laser beam. The radiation source for the interferometry is a cw argon ion laser (Coherent, Model Innova 100–10) operated at an emission wavelength of 514.5 nm. The interference fringes are observed with the streak camera. To avoid damage to the streak camera due to continuous illumination by the argon laser beam, a mechanical shutter and an acousto-optic modulator (AOM) are used to extract pulses of $\sim$10 μs duration of the argon laser beam synchronized to the triggering of the Nd:YAG laser. The first order diffracted beam of the AOM is used for the interferometer, whereas the zeroth and higher orders are blocked by an aperture (see A in Fig. 3). The telescope (L2 and L3 in Fig. 3) serves to adjust the diameter of the illuminated area at the location of the plasma. To cover the total plasma geometry during the expansion phase, an illumination diameter of 20 mm was choosen. The second

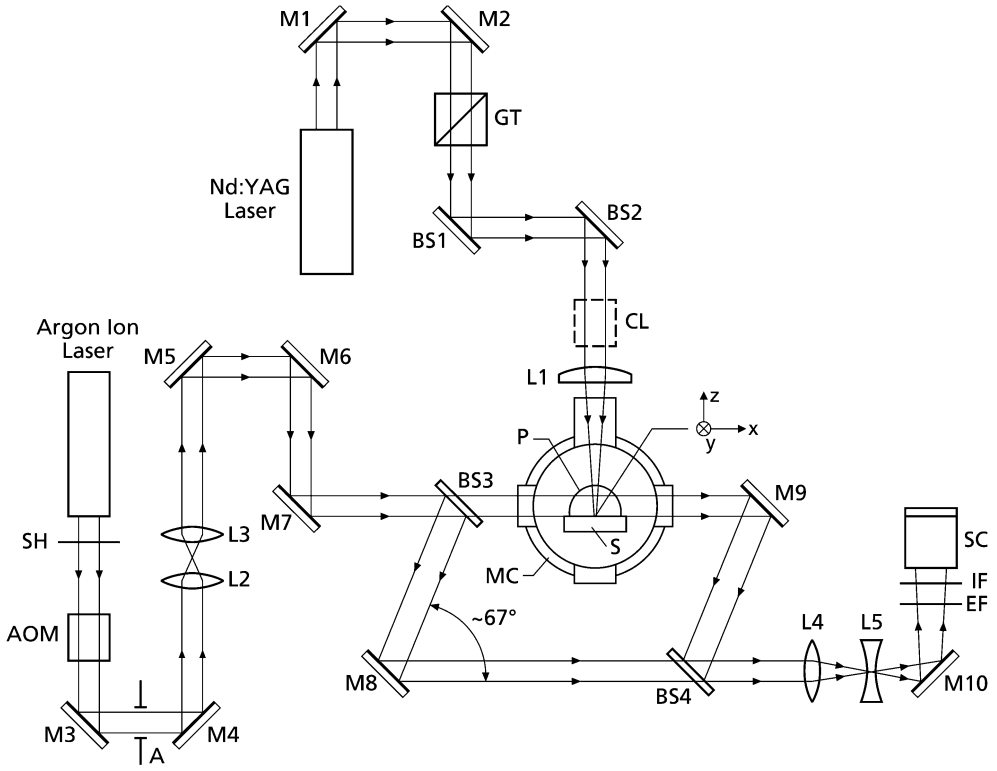

Fig. 3 Experimental set-up for the interferometric measurement of the laser-induced plasma. SH, Shutter; AOM, acousto-optic modulator; A, aperture; BS1 to BS4, beam splitters; MC, measuring chamber; EF, edge filter; IF, interference filter. For further abbreviations see Fig. 1.

telescope (L4 and L5), and the internal optic of the streak camera, form an image of the plasma on the photocathode. The beam deviation of the argon laser beam due to refractive index gradients in the interaction region of the Nd:YAG laser beam may cause uncertainties in the Abel inversion of the interferograms: however, accurate results are achieved by proper imaging of the plasma plane on the photocathode of the streak camera.[17] The interference filter has a maximum transmission at the wavelength of the argon ion laser and a spectral width of 10 nm (FWHM). The edge filter (Schott, type OG 515) attenuates additionally the intense emission of the laser-induced plasma.

The Nd:YAG laser, shutter, AOM and streak camera are synchronized using a personal computer as master trigger and three digital delay generators. Before the start of each measurement a minimum of 50 flashlamp discharges of the laser are activated to stabilize the pulse energy to a standard deviation of 2%.

3. Results and discussion

3.1. Framing and streak photography

The framing and streak images shown in this section are gained with the set-up shown in Fig. 2. Figs. 4 and 5 show framing photographs of the evolving plasma induced by a 2 × 40 mJ

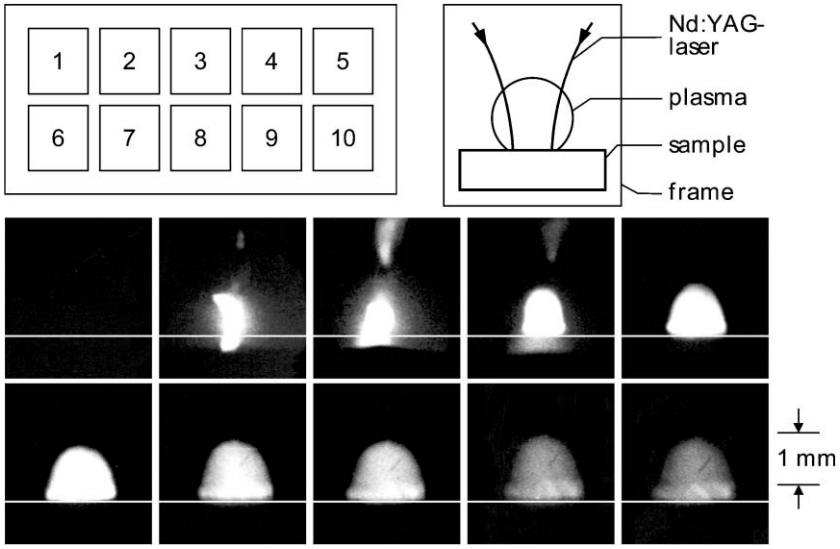

Fig. 4 Framing images of the laser-induced plasma after the first pulse of a double pulse. Exposure time 10 ns per frame, time between subsequent frames 50 ns. The time sequence of the frames is shown on the top left with the numbers 1–10. The view detected by the frames is illustrated schematically on the top right. The white horizontal line in each frame indicates approximately the position of the sample surface. Laser parameters: 2 × 40 mJ, interpulse separation 6 μs.

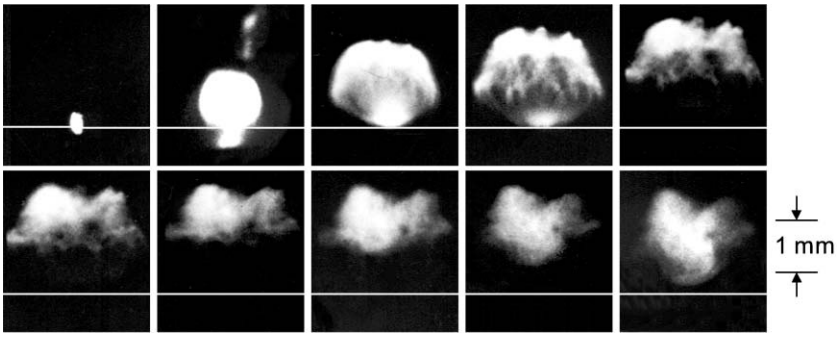

Fig. 5 Framing images of the laser-induced plasma after the second pulse of a double pulse. Experimental settings and arrangement of frames are as for Fig. 4.

laser double pulse in air at 1 bar. The streak camera is operated with a framing rate of 2×10^7 frames s^{-1}, *i.e.*, the temporal separation between subsequent frames amounts to 50 ns. The exposure time per frame is 10 ns. The magnification and the setting of the aperture of the microscope are kept constant to assure comparability of the recordings. Fig. 4 shows the frames after the first pulse of the double pulse. The first pulse reaches the sample between frames 1 and 2. (Numbers refer to the sequence of frames as indicated on the top left of Fig. 4. The arrangement of frames shown in Fig. 4 was choosen according to the usual orientation of the time axis from left to right. The original arrangement of the frames yielded by the streak camera is different.) Frames 2–4 are overexposed due to the high luminosity of the plasma at this phase. Fig. 5 shows the frames after the second pulse of the double pulse. The second pulse of the double pulse reaches the sample at the exposure of frame 1 (frame numbering as for Fig. 4).

The plasma geometry and dynamics observed in Figs. 4 and 5 differ significantly from each other. After the first pulse a nearly hemispherical plasma geometry appears staying in contact with the sample surface for times up to 400 ns after arrival of the first laser pulse. The extension of the plasma in the direction of the laser beam axis amounts to $\sim$1 mm (frame 5 corresponding to an elapsed time of 150 ns after the first visible plasma emission in frame 2). After the second pulse the plasma emission starts at the sample surface (see frame 1 in Fig. 5). This is a clear indication that the second laser pulse primarily interacts with the sample surface and not with a residual plasma originating from the first pulse. The plasma then splits into two regions, where one region lasts at the sample surface and dissappears after about 100 ns. The other region attains a layer-like shape, propagating towards the incoming laser beam. At $\sim$150 ns after the irradiation of the second pulse of the double pulse an inhomogeneous distribution of the luminosity in this layer is observed, looking like a turbulent structure, which tends to decrease at later times. After 200 ns the expansion towards the incoming laser beam stops. After 350 ns the luminous plasma starts to expand in the backwards direction towards the sample surface. At 450 ns the plasma shows a more homogeneous luminosity distribution and its shape differs significantly from the one observed in the time interval between 150 ns and 250 ns. The plasma has nearly reached the sample surface again.

The further temporal development can be observed by streak photographs as shown in Fig. 6. The observation geometry is the same as for Figs. 4 and 5. The streak velocity amounts to 50 ns mm^{-1} on the screen of the streak camera. The time scale runs from left to right. (In the original streak images delivered from the streak camera the time scale ran from right to left. These images are presented here side-inverted according to the usual direction of the time axes.) The white line illustrates the position of the surface of the sample. The luminous regions beneath the white line are due to an overexposure of the streak images for times close to the arrival of the laser pulse. The

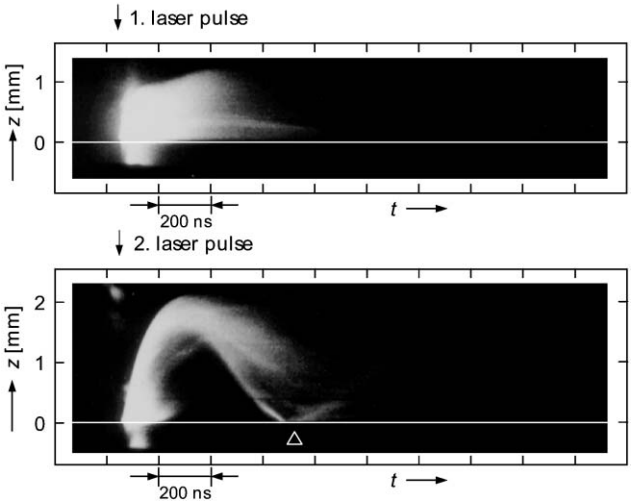

Fig. 6 Streak photographs after first and second laser pulse of a double pulse. Experimental parameters are the same as for Fig. 4.

upper image shows the laser-induced plasma after the first pulse, the lower image shows the plasma after the second pulse. After the first pulse, the plasma stays in contact with the sample surface, while the boundary of the luminous plasma expands to about 1 mm above the sample, as observed in the framing images of Fig. 4. The luminous layer evolving after the second pulse starts at the sample surface and expands up to a distance of about 2 mm from the sample surface. After 300 ns the front of the luminous layer changes direction and propagates back towards the sample. Approximately 600 ns after the irradiation of the second laser pulse, the luminous front again reaches the sample surface (marked by a white triangle in the lower image of Fig. 6). At the surface a partial reflection of the plasma front is visible. The observed dynamics of the plasma expansion after the second pulse is a clear indication that the first laser pulse has led to a transient modification of the ambient particle density above the sample, thus enabling a greater expansion of the sample material ablated by the second pulse. The observed reflection-like behaviour of the luminous front at about 300 ns after the second laser pulse may be caused by a radially increasing particle density in the surrounding atmosphere as a result of the interaction of the first laser pulse. Streak photographs taken with a greater aperture of the microscope show that for times beyond 1 μs after the second laser pulse the luminosity of the plasma becomes more and more homogeneous and the structure and geometry of the plasma stays nearly constant for more than 5 μs.

In the time range shown in Figs. 4–6 the emission spectrum of the plasma changes from a continuum emission at early times to pronounced line emissions after about 800 ns.[6] The exponential decay of the continuum emission can be described by a decay time constant of about 90 ns corresponding to the

time range covered by the frames 2 and 3 of Fig. 4 and frames 1, 2 and 3 of Fig. 5.

Framing and streak images of Figs. 5 and 6 show clearly that the dominant effect of the second pulse is again an interaction with the sample surface and not a re-heating of a residual plasma above the sample originating from the first pulse. In a simplified approach we do not consider the non-linear character of the interaction of the laser beam with the residual plasma, which may lead to heating and ionisation processes. The absorption of laser radiation in a plasma can then be described by the absorption coefficient using the following formula,[18] assuming $\nu_c \ll \omega$ and $\omega_p \ll \omega$:

$$\alpha = \frac{\nu_c \omega_p^2}{c_0 \omega^2 \sqrt{1 - \frac{\omega_p^2}{\omega^2}}} \quad (1)$$

where ν_c is the collision frequency, ω_p the plasma frequency and ω the laser frequency. For this estimate we neglect absorption by microscopic particulates originating from condensed iron vapour or solidified melt droplets thrown out of the interaction region by the first pulse. The collision frequency ν_c is given by $\nu_c = \nu_{ei} + \nu_{en}$, where ν_{ei} is the electron-ion collision frequency and ν_{en} the electron-neutral collision frequency. The electron-ion collision frequency ν_{ei} can be estimated using the formula given in ref. 19 for the electron-ion momentum transfer in a plasma using the screened Rutherford cross section and assuming a Maxwellian electron distribution. The electron-neutral collision frequency is estimated by taking the geometric cross section of neutral iron atoms. With the following plasma parameters determined spectroscopically at a time delay of 1 μs after a single pulse of 80 mJ: electron density $n_e = 7 \times 10^{16}$ cm^{-3}, neutral iron density $n_{Fel} = 6 \times 10^{16}$ cm^{-3}, electron temperature $T_e = 8300$ K, we obtain $\nu_{ei} = 1.3 \times 10^{12}$ s^{-1} and $\nu_{en} = 1.4 \times 10^9$ s^{-1}. Using relation (1) the estimated absorption coefficient due to ablated material originating from the first pulse amounts to $\alpha = 0.3$ m^{-1}. Taking as an upper limit a plasma dimension of 5 mm, this corresponds to a transmission of more than 99% of the irradiated laser intensity of the second pulse. In this case a dominant part of the laser energy may propagate to the sample surface again where it interacts with the pre-ablated sample surface. Hence, the plasma emission induced by the second pulse should start at the sample surface, which is consistent with the experimental observations of Figs. 5 and 6.

The expansion of the laser-induced plasma can be described by the Sedov-model for shock waves after a strong explosion in a homogeneous atmosphere.[20,21] A dimensional analysis leads to the following relationship for the expansion z of the shock wave as a function of time t:

$$z = \lambda_0 (E_0/\rho_0)^{\frac{1}{2+\xi}} t^{\frac{2}{1+\xi}} \quad (2)$$

where E_0 is the energy deposited in a small volume and ρ_0 is the density of the homogeneous undisturbed ambient gas, λ_0 depends on the specific heat ratio of the surrounding gas and ξ describes the geometry of the energy release and the shock wave expansion with $\xi = 3$ for a point-like energy release and a spherical shock wave expansion and $\xi = 1$ for a planar shock wave expansion. Hence, for a spherical shock wave the expansion should follow the relation $z \propto t^{0.4}$ and for a planar expansion $z \propto t^{0.66}$. The exponent of t is always expected to be twice that of (E_0/ρ_0).

To determine the expansion velocity of the luminous plasma with a higher accuracy we have taken streak images of the expanding plasma with streak velocities of 1 ns mm^{-1} and 5 ns mm^{-1}, while keeping the other experimental parameters constant. Fig. 7 shows a double-logarithmic plot of the determined expansion velocities after the first and the second laser pulse of a double pulse. The time zero was chosen at the start of the plasma emission detected in the streak images. The error

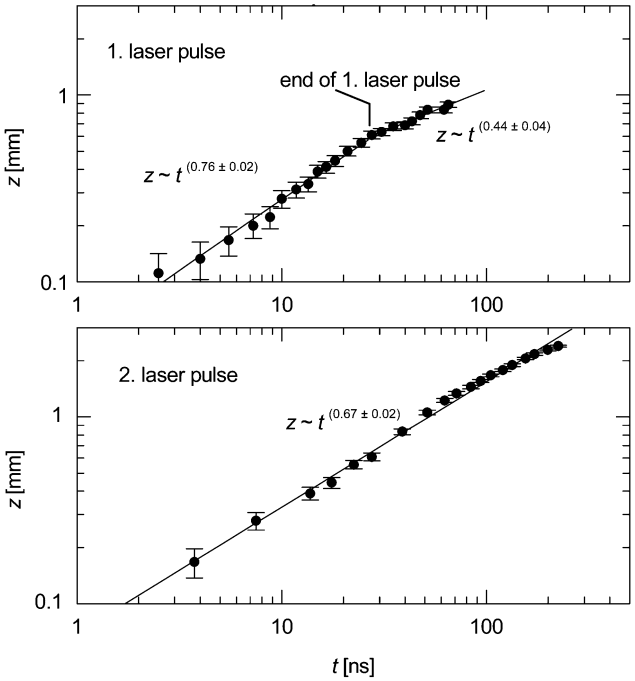

Fig. 7 Height z of the luminous plasma front above the sample surface as a function of time determined from side-on streak images. Top: after the first laser pulse; bottom: after the second laser pulse. Experimental parameters are the same as for Fig. 4.

bars in the z-direction indicate the reading error in determining the front position on the enlarged streak images. Uncertainties on the time axis are caused by deviations from the nominal streak velocity, which are specified to be less than 5%, and by reading errors. The corresponding error bars are not shown in Fig. 7 since they are significantly smaller than those in the z-direction. After the first pulse two regions of different dynamics can be distinguished. For times up to 25 ns after the start of the interaction of the first laser pulse the data points can be fitted by a linear regression described by the function $z \propto t^{(0.76 \pm 0.02)}$. A linear fit to the data points after 25 ns yields $z \propto t^{(0.44 \pm 0.04)}$. Under the assumption that the luminous plasma front coincides with the position of the shock front at the early expansion phase, we can compare the determined dynamics with the prediction of Sedov's model. For times $\leqslant 25$ ns Sedov's model cannot be applied, since the laser pulse still persists and couples energy into the interaction region. Beyond 25 ns the determined exponent is close to the theoretical value for a spherical expansion of a shock front. For the second laser pulse the determined data points are shown in the lower diagram of Fig. 7. Applying a single fit using the function $z \propto t^{\beta}$ yields an exponent of $\beta = 0.67 \pm 0.02$, which is consistent with a planar shock front expansion. (A close look at the data points in the lower diagram of Fig. 7 shows that there might be a small change in the dynamics after a time of about 60 ns. Applying the fit only to the data points with $t > 60$ ns yields $\beta = 0.53 \pm 0.02$. However, the change in the dynamics after the second pulse at a time of about 60 ns is significantly smaller than the one oberved at about 25 ns after the first laser pulse.) These values indicate different expansion geometries for the plasmas induced by the first and the second laser pulse and are in qualitative agreement with the results of the framing images shown in Figs. 4 and 5.

The derivatives of the regression curves of Fig. 7 yield the expansion velocities of the luminous plasma front in the z-direction. In the time interval from $t = 30$ ns to $t = 60$ ns after the first laser pulse this velocity decreases from 0.8×10^6 cm s^{-1} to 0.6×10^6 cm s^{-1} (corresponding to Mach numbers of 23 and 17), whereas in the same time interval after the second laser pulse the expansion velocities are 1.5×10^6 cm s^{-1} and

1.2×10^6 cm s^{-1} respectively. Hence, after the second pulse the expansion is, by about a factor of 2, faster than after the first pulse.

3.2. Interferometry of shock wave propagation

The experimental setup shown in Fig. 3 enables the observation of changes of the refractive index n caused by the expanding plasma in the measuring arm of the Mach–Zehnder interferometer. In a first step, without the laser-induced plasma, the mirrors of the interferometer are tilted to adjust the number and orientation of the interference fringes. We have chosen a fringe orientation parallel to the sample surface. The slit of the streak camera crosses these fringes perpendicularly. Fig. 8 shows streak images of the interferograms for a laser double pulse with 2×80 mJ, $\Delta t = 6$ μs and $\Delta s = 5$ mm. The sample surface is located at $z = 0$ mm. The expanding plasma and shock front leads to a displacement of the interference fringes. After the first laser pulse a disturbance of the fringe pattern propagates in the positive z-direction. At the leading edge of this disturbance a strong displacement of the interference fringes towards the sample surface is observed. Reference measurements with glass plates in the measuring arm of the interferometer show that this direction of fringe displacement corresponds to an increased index of refraction. Hence the displacement of the fringes observed at the leading edge of the expanding fringe disturbance is attributed to an increased particle density caused by the shock wave. After the second laser pulse an analogue displacement of the interference fringes is observed at the leading edge of the evolving disturbance in the fringe pattern, indicating the formation of a second shock front propagating behind the shock front induced by the first laser pulse. The reflection-like behaviour of the luminous plasma observed in Fig. 6 at about 300 ns after the impact of the second pulse does not show up in a corresponding structure of the fringe patterns observed in Fig. 8. A potential reason might be a too small change in the refractive index caused by the back-travelling plasma, which cannot be resolved by the set-up used.

For a comparison of the experimental data with the Sedov model, the expansion z of the shock front as a function of time t is shown in a double-logarithmic plot in Fig. 9.

The distortion of the interference fringes can be detected clearly for more than 12 μs after the laser pulse interaction (see Fig. 8 bottom, shock front induced by the first laser pulse at about $z = 7$ mm) in contrast to the luminosity of the plasma, which can be observed for a few microseconds only. The

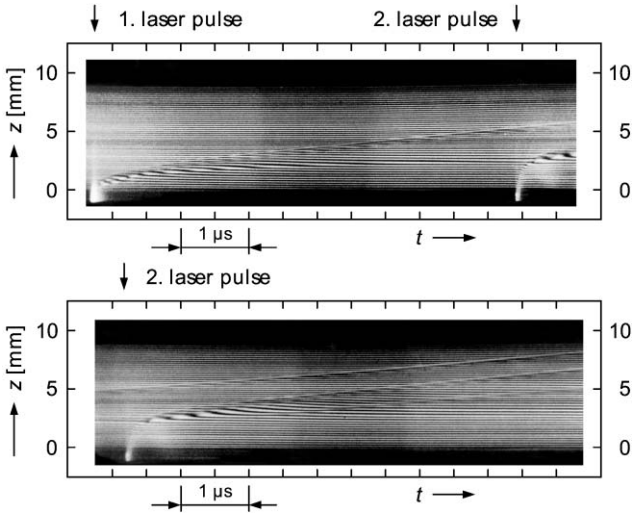

Fig. 8 Interferograms registered with the streak camera after the first and second laser pulse of a double pulse. Laser parameters: 2×80 mJ, interpulse separation 6 μs, $p_0 = 1013$ mbar.

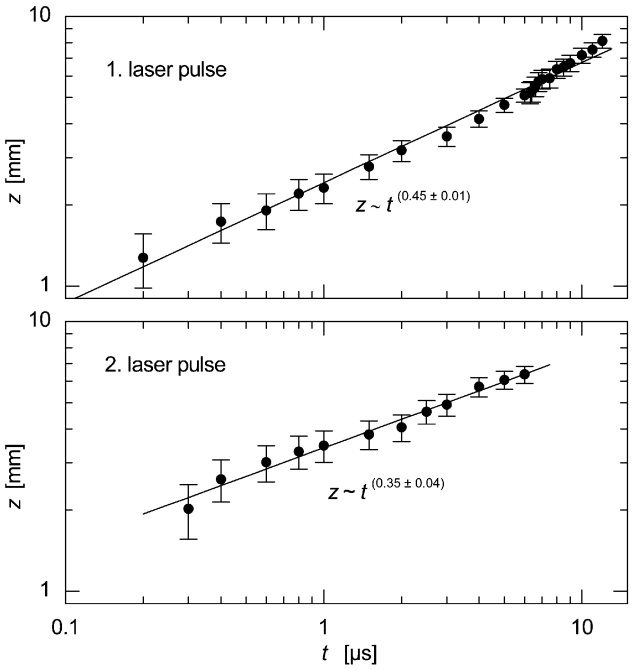

Fig. 9 Height z of the shock front above the sample surface as a function of time determined from interferograms observed in side-on direction with the streak camera, *cf.*

exponent describing the expansion of the shock front in the time range from 200 ns to 12 μs after the first pulse amounts to 0.45 ± 0.01. This result agrees with the exponent determined from the streak images of the luminous plasma at the early times between 30 ns and 65 ns after the first laser pulse, *cf.* Fig. 7. The time exponent of the shock front expansion after the second laser pulse is 0.35 ± 0.04 and hence it is significantly smaller than the one determined from the luminous front at early times, *cf.* Fig. 7.

For the determination of the time exponent for the shock front propagation after the first laser pulse, functions of the following form are fitted to the measuring data:

$$z = At^a \tag{3}$$

Since the shock front propagates into an undisturbed ambient atmosphere the pre-conditions of Sedov's model are fulfilled and a comparison of eqn. (3) with eqn. (2) yields the following relations: $a = 2/(2 + \xi)$ and $A = \lambda_0(E_0/p_0)^{a/2}$. For the latter parameter the relation $A \propto (E_0/p_0)^{a/2}$ also holds, where p_0 is the ambient pressure, which can be changed in the experiment, *cf.* Fig. 3. In the following we assume that the energy E_0 deposited locally is proportional to the irradiated laser pulse energy E_1 (E_1 denotes the pulse energy of a single pulse or the pulse energy of the first pulse of a double pulse). The fit parameters A and a are determined for measurements with the following sets of parameters: (a) single laser pulses with $E_1 =$ 20 mJ, 40 mJ, 80 mJ, 120 mJ and 160 mJ at $p_0 = 1$ bar ambient pressure; (b) single laser pulses with $E_1 = 40$ mJ at ambient pressures of $p_0 = 100$ mbar, 500 mbar and 1013 mbar. For these parameters the determined exponent a varies between 0.36 and 0.50, with an average value of $\bar{a} = 0.43 \pm 0.05$. This value agrees with the expected exponent of 0.44 for a spherical shock front propagation according to Sedov's model. Relation (3) describes well the dependence of the shock wave position as a function of time for distances of up to 7 mm from the sample surface, which is still below the critical radius[21] $r_c = (E/p_0)^{1/3}$, which amounts to $r_c = 9.3$ mm for $E = 80$ mJ and $p_0 =$ 1013 mbar. At r_c the counterpressure of the ambient gas can no longer be neglected and the self-consistent solution of the problem of a strong explosion no longer holds.

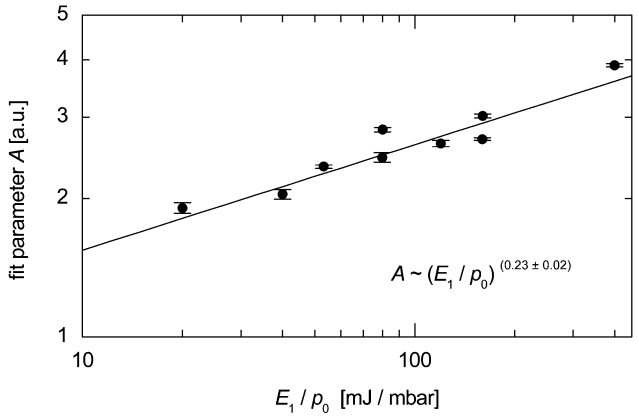

Fig. 10 Fit parameter A as a function of the ratio of the laser pulse energy E_1 and the ambient pressure p_0 for the first laser pulse.

Fig. 10 shows the values of the fit parameter A determined for the parameter sets described above in a double-logarithmic plot. The linear regression shown in Fig. 10 yields: $A \propto (E_1/p_0)^{0.23 \pm 0.02}$. As expected by the Sedov model, the exponent is about half of $\bar{a}$. Hence the dynamics of the shock front propagation after the first laser pulse can be described in a wide range of laser pulse energies and ambient pressures by Sedov's model for a spherical expansion.

For the description of the expansion of the shock wave after the second laser pulse, we use in analogy to relation (3) the following function: $z = Bt^b$. Since the ambient atmosphere is not homogeneous for the second shock wave the parameters B and b cannot be interpreted with respect to eqn. (2). The following measuring parameters were used to determine B and b: (a) double pulses with $E_1 = E_2$ (E_2 denotes the pulse energy of the second pulse of a double pulse) and $E_2 = 20$ mJ, 40 mJ, 60 mJ, 80 mJ and 100 mJ at $p_0 = 1013$ mbar ambient pressure; (b) double pulses with $E_1 = E_2 = 40$ mJ at ambient pressures of $p_0 = 100$ mbar, 500 mbar and 1013 mbar. The determined fit parameter b varies between 0.27 and 0.41, with an average value of $\bar{b} = 0.32 \pm 0.05$. Fig. 11 shows the determined parameter B as a function of the laser pulse energy of the second pulse E_2 at a pressure of $p_0 = 1013$ mbar (pressure in the ambient atmosphere before the impact of the first pulse). A regression curve yields: $B \propto (E_2)^{(0.30 \pm 0.02)}$. The parameter B is not plotted as a function of (E_2/p_0) since there is no homogeneous pressure distribution in the interaction region at the time the second laser pulse is irradiated on to the sample. The determined exponent is approximately equal to $\bar{b}$. This behaviour differs significantly from the shock wave propagation after the first laser pulse.

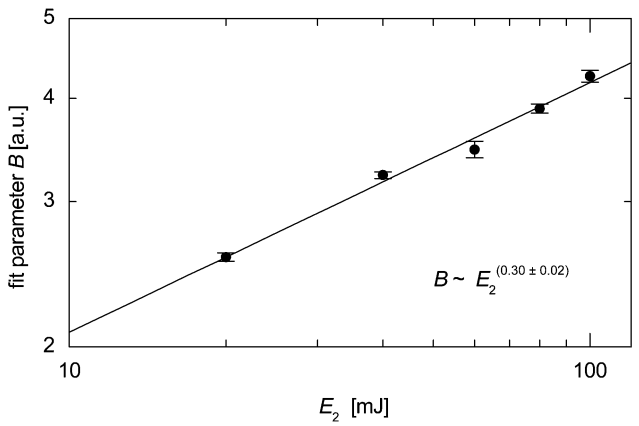

Fig. 11 Fit parameter B as a function of the ratio of the energy E_2 of the second laser pulse at an initial ambient pressure of $p_0 = 1013$ mbar.

The propagation of shock waves in an inhomogeneous atmosphere was described by Sedov assuming the following relation for the density variation of the ambient atmosphere by a power law:[20]

$$\rho = \rho(r) = Dr^{-\varphi} \quad (4)$$

where D is a positive constant, r is the radius and φ is a dimensionless constant. The propagation of a spherical shock wave as a function of time is then given by the following power law:

$$r \propto t^{2/(5-\varphi)} \quad (5)$$

Taking the experimentally determined exponent for the shock wave after the second pulse and relation (5), we obtain $\varphi = -1.25$. Eqn. (4) then yields $\rho(r) \propto r^{1.25}$, which describes a density increasing radially from the center. Whereas the first shock wave propagates into a spatially homogeneous ambient atmosphere, the second shock wave encounters, as a result of the interaction of the first laser pulse, a locally rarefied ambient atmosphere, allowing for higher propagation velocities of the second shock wave.

3.3. Index of refraction of laser-induced plasma

The index of refraction caused by the laser-induced plasma is determined from the interference patterns detected in the framing mode of the streak camera. Figs. 12 and 13 show framing images of the interference patterns after the first and the second laser pulse of a 2 × 80 mJ double pulse and an ambient pressure of $p_0 = 1013$ mbar. The framing rate is 10^6 s^{-1}, corresponding to a time separation between subsequent frames of 1 μs. The exposure time amounts to 200 ns per frame. For a better use of the image format of the streak camera the camera is rotated by 90 degrees around the axis of observation. The mutual distance between the interference fringes is increased in relation to the one chosen for the streak images in the previous section to simplify the evaluation of the interferograms. The geometry and sequence of the frames is shown on the right side of Fig. 12. The time of irradiation of the laser pulses cannot be determined exactly from the framing images. In Fig. 12 the first pulse arrives at the sample between the frames nos. 1 and 2, and the second pulse between frames 7 and 8. In Fig. 13, the second pulse hits the sample between frame nos. 1 and 2.

The boundaries of the displaced interference fringes show a well defined hemispherical shape. At the front of the shock wave the fringes are displaced towards the sample surface, which is due to the increase of the refractive index caused by the compressed air and sample particles. Inside the sphere, defined by the leading edge of the shock wave, the fringes are displaced in the opposite direction, *i.e.*, towards the positive z-direction, compared with their original position. This displacement corresponds to a refractive index <1, indicating the presence of free electrons and/or a depletion of the ambient atmosphere. The fringe displacements are symmetrical with respect to the z-axis, hence the method of Abel inversion can be applied to determine the refractive index distribution.[22]

The fringe displacement is given by:

$$\delta(y,z,t) = \frac{1}{\lambda}\int_{\mathrm{p}} (n_{\mathrm{p}} - n_{\mathrm{a}})\,\mathrm{d}x \quad (6)$$

where x, y, z are the coordinates shown in Fig. 3, λ is the wavelength of the argon ion laser, n_{p} is the refractive index of the plasma and n_{a} is the refractive index of the ambient atmosphere in the reference arm of the interferometer. The integration runs along the line of sight across the plasma volume. The refractive index of the plasma can be described by the following

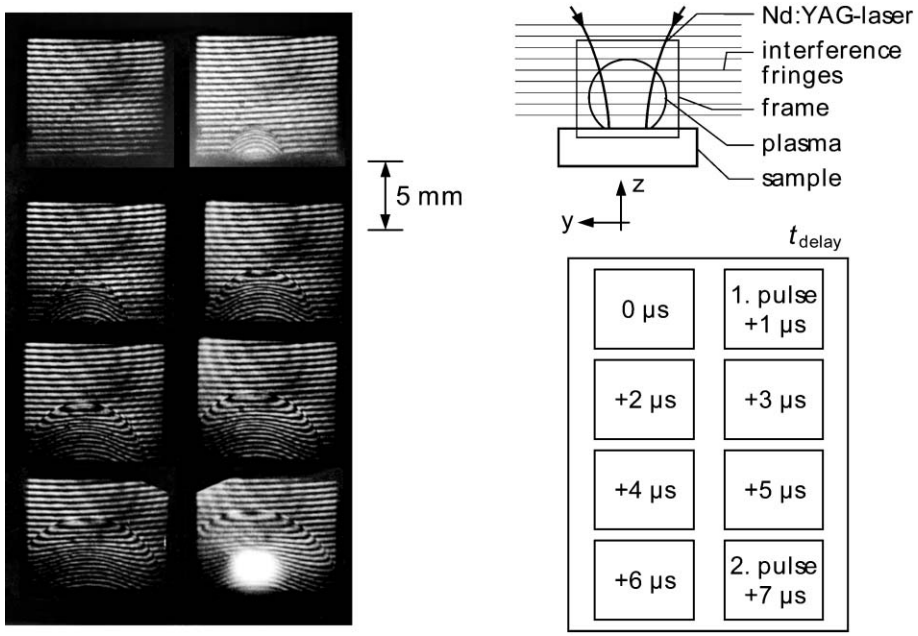

Fig. 12 Framing images of inteferograms detected in a time interval between the first and the second laser pulses of a double pulse. In the upper right a schematic view of the orientation of the fringes relative to the plasma and the sample is shown. The diagram in the lower right shows the temporal sequence of the frames with the delay times t_{delay}, starting at 0 µs for the first frame. Experimental parameters are the same as for Fig. 8.

relation:[22]

$$n_p - 1 = -\frac{e^2\lambda^2}{8\pi^2 m_e c^2 \varepsilon_0} N_e + \sum_j 2\pi N_j \alpha_j \qquad (7)$$

where N_e is the electron density, N_j are the densities of neutral atoms and ionic species in the plasma and α_j the polarizabilities. The polarizability of atomic iron[23] is $\alpha_{FeI} = 13 \times 10^{-30}$ m^{-3}. The contribution of the iron atoms to the refractive index can then be estimated with eqn. (7): $n_{FeI} - 1 = +8.2 \times 10^{-23} N_{FeI}$, where N_{FeI} is the particle density of atomic iron in cm^{-3}. The contribution of the free electrons amounts to $n_e - 1 = -12 \times 10^{-23} N_e$, with N_e in cm^{-3}. With an average degree of ionization in the plasma, determined spectroscopically, of 90% the ratio $|n_{FeI} - 1|/|n_e - 1|$ amounts to 0.08, hence the contribution of the atomic iron particles can be neglected. No data for the polarizability of singly ionized iron atoms have been found in the literature. However, calculations of polarizabilities for the transition element copper showed that the polarizability of a copper ion is less than one-tenth of the value calculated for copper atoms.[24] Assuming that similar relations hold for iron we expect only a small contribution of the iron ions to the refractive index, which is in the order of the one estimated for the iron atoms.

A reduction of the ambient gas particle density behind the shock wave will lead to a reduced refractive index. The order of magnitude of this effect is estimated assuming that the shock wave reduces the ambient gas particle density completely, *i.e.*, the shock wave leaves a vacuum behind. Under this simplified assumption the ratio of the fringe displacements due to vacuum δ_v and free electrons δ_e amounts to: $\frac{\delta_v}{\delta_e} = |1 - n_a|/|n_e - n_a| = 0.7$ for $n_a = 1.000\,277\,9$, $\lambda = 514.5$ nm and $N_e = 10^{18}$ cm^{-3}. If a complete displacement of the ambient

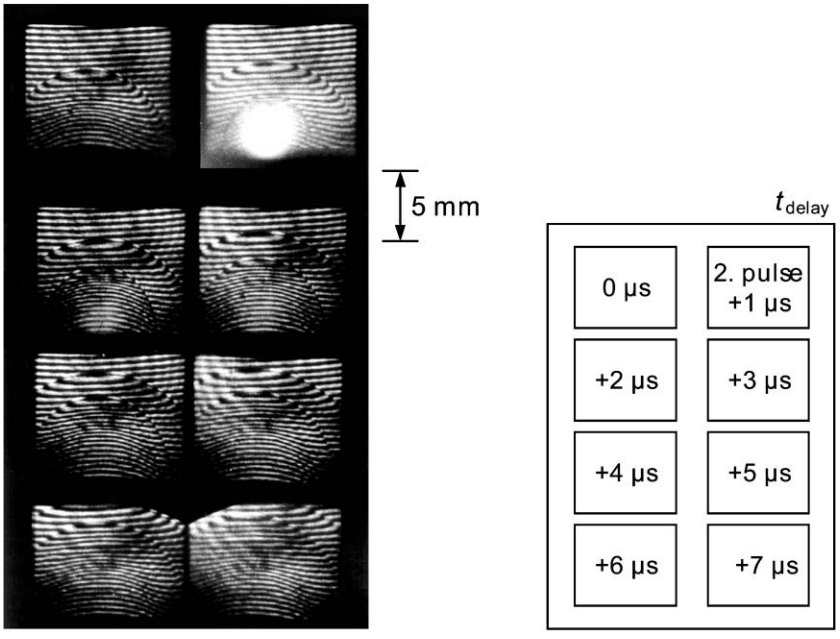

Fig. 13 Framing images of inteferograms detected after the second laser pulse of a double pulse. All other experimental parameters are the same as for Fig. 12.

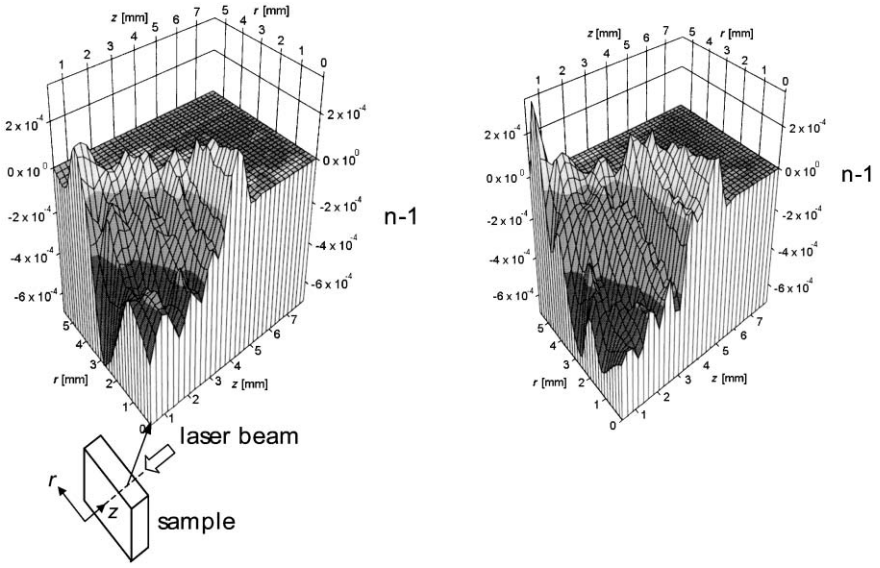

Fig. 14 Refractive index distribution determined from the framing interferograms. Left: 4 μs after a single 80 mJ laser pulse. Right: 5 μs after a single 80 mJ laser pulse.

atmospheric particle density occurs, then the expected fringe shift is of the same order of magnitude as the one expected by the free electrons of the plasma. Since both effects go into the same direction, the experimentally determined fringe shifts can only be attributed to the free electrons of the plasma by the ratio $\frac{\delta_e}{\delta_e+\delta_v}=0.6$.

Fig. 14 shows the determined distribution of the refractive index 4 μs (left) and 5 μs (right) after the irradiation of one 80 mJ laser pulse. The formation of the shock front in a spherical geometry can be clearly seen by the values of the refractive index $n > 1$. Behind the shock front a volume of reduced refractive index becomes visible. Fig. 15 shows refractive index distributions 2 μs after a single 80 mJ laser pulse (left) and after the second pulse of a 2 × 40 mJ double pulse (right). The formation of two concentric shock waves can be seen in the right diagram, where the second shock wave is weaker than the first. Interpreting the central region with $n < 1$ as the plasma volume, the volume ratio amounts to 3.3, *i.e.*, the plasma volume after the double pulse is by a factor of 3.3 greater than in the case of the single pulse (for the same total laser pulse energy irradiated). Framing interferograms taken at a reduced ambient pressure of 500 mbar show a reduced depth of the refractive index trough.

In the following we assume that only the free electrons lead to the reduced refractive index region with $n < 1$; then the relation (7) can be used to calculate the electron density distribution. Fig. 16 shows the result. At the centre of the plasma sphere the electron density attains a value of $\sim 3 \times 10^{18}$ cm^{-3}. The estimated relative error is 20%. Taking into account the above discussed reduction of the ambient gas particle density behind the shock wave, the electron density is only ~60% of this value, *i.e.*, 2×10^{18} cm^{-3}. The electron density determined interferometrically after a single pulse of 80 mJ and 2 μs is about the same. Comparing these values with those gained from Stark broadened atomic iron lines measured by spatially integrating the whole plasma emission[6] shows that the interferometric values are more than an order of magnitude greater. A potential reason for this discrepancy could be that the Stark broadening of iron atoms (Fe I line at 538.337 nm) was measured, hence the outer regions of the plasma contributed predominantly to the spectroscopic signals, where the electron density is lower than in the centre.

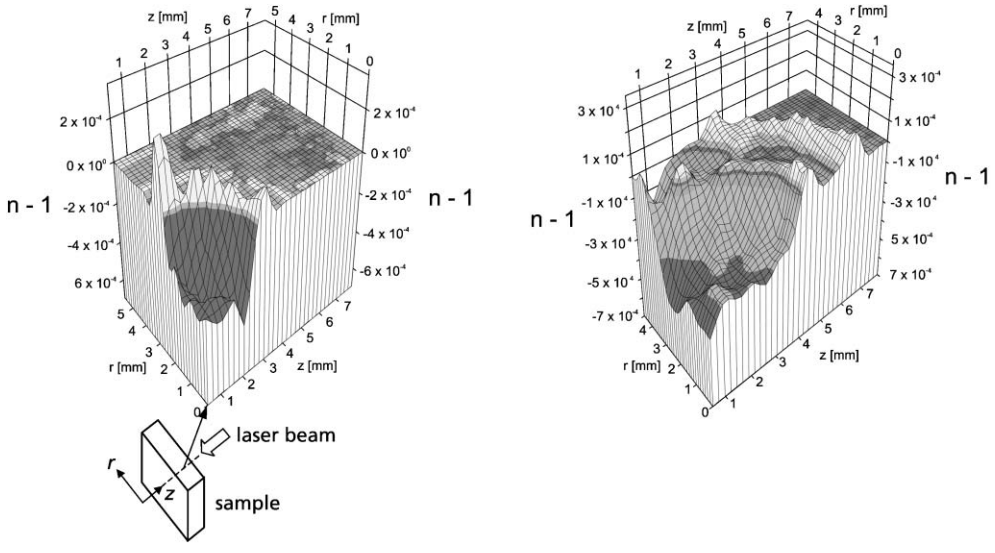

Fig. 15 Refractive index distribution determined from the framing interferograms. Left: 2 μs after a single 80 mJ laser pulse. Right: 2 μs after the second pulse of a 2 × 40 mJ double pulse.

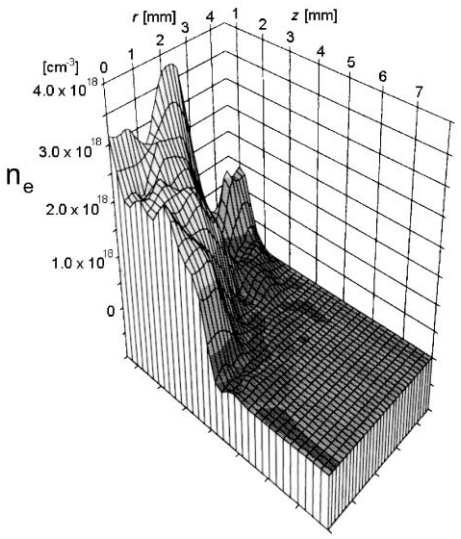

Fig. 16 Electron density distribution calculated from Fig. 15, right, assuming that the refractive index inside the second shock wave is caused by free electrons only.

Conclusions

The investigations have shown that the effect of collinear double pulses is a local transient reduction of the particle density in the vicinity of the sample surface caused by the first pulse. The second pulse interacts predominantly with the sample surface. No re-heating of a residual plasma from the first pulse was observed. The material ablated by the second pulse expands faster into the cavity of reduced particle density originating from the first pulse attaining a significantly enlarged plasma volume. The electron densities are approximately the same for single and double pulses of the same total energy. The larger plasma volume and the fact that the mass ablated using double pulses is also increased significantly[6] favours a more intense and longer lasting emission of element specific radiation to be used for LIBS analysis.

References

1 L. Berman and P. Wolf, *Appl. Spectrosc.*, 1998, **52**, 438–442.
2 H. Zhang, F. Yueh and J. Singh, *Appl. Optics*, 1999, **38**, 1459–1466.
3 F. Wallis, B. Chadwick and R. Morrison, *Appl. Spectrosc.*, 2000, **54**, 1231–1235.
4 D. Anglos, *Appl. Spectrosc.*, 2001, **55**, 186A–205A.
5 M. Kurihara, K. Ikeda, Y. Izawa, Y. Deguchi and H. Tarui, *Appl. Optics*, 2003, **42**, 6159–6165.
6 R. Sattmann, V. Sturm and R. Noll, *J. Phys. D: Appl. Phys.*, 1995, **28**, 2181–2187.
7 A. Pichahchy, D. Cremers and M. Ferris, *Spectrochim. Acta, Part B*, 1997, **52**, 25–39.
8 V. Sturm, L. Peter and R. Noll, *Appl. Spectrosc.*, 2000, **54**, 1275–1278.
9 F. Colao, V. Lazic, R. Fantoni and S. Pershin, *Spectrochim. Acta, Part B*, 2002, **57**, 1167–1179.
10 L. St.-Onge, V. Detalle and M. Sabsabi, *Spectrochim. Acta, Part B*, 2002, **57**, 121–135.
11 S. Klimentov, S. Garnov, T. Kononenko, V. Konov, Pl. Pivovarov and F. Dausinger, *Appl. Phys. A*, 1999, **69**, S633–S636.
12 D. Stratis, K. Eland and S. Angel, *Appl. Spectrosc.*, 2001, **55**, 1297–1303.
13 D. Stratis, K. Eland and S. Angel, *Appl. Spectrosc.*, 2000, **54**, 1270–1274.
14 A. Kuwako, Y. Uchida and K. Maeda, *Appl. Optics*, 2003, **42**, 6052–6056.
15 R. Noll, R. Sattmann, V. Sturm, S. Lüngen and H.-J. von Wachtendonk, *Stahl und Eisen*, 1997, **117**, 57–62 (in German).
16 L. Peter, V. Sturm and R. Noll, *Appl. Optics*, 2003, **42**, 6199–6204.
17 C. M. Vest, *Appl. Optics*, 1975, **14**, 1601–1606.
18 P. Mulser, *Z. Naturforsch.*, 1970, **25a**, 282–295.
19 A. Anders, *A Formulary for Plasma Physics*, Akademie-Verlag, Berlin, 1990, p. 51.
20 L. I. Sedov, *Similarity and Dimensional Methods in Mechanics*, Gostekhizdat, Moscow, 4th edn., 1957. English transl. ed. M. Holdt, Academic Press, New York, 1959.
21 Y. B. Zel'dovich and Y. P. Raizer, *Physics of Shock Waves and High-Temperature Hydrodynamic Phenomena*, eds. W. Hayes and R. Probstein, Academic Press, New York, 1966, vol. I.
22 R. Boxmann, *J. Appl. Phys.*, 1974, **45**, 4835–4846.
23 S. Fraga, J. Karwowski and K. Saxena, *Atomic and Nuclear Data Tables*, 1973, 12.
24 S. Fraga, K. Saxena and B. Lo, *At. Data*, 1971, **3**, 323–332.